Joule

CellPress

Article

High-Performance Thermoelectrics from Cellular Nanostructured $Sb_2Si_2Te_6$

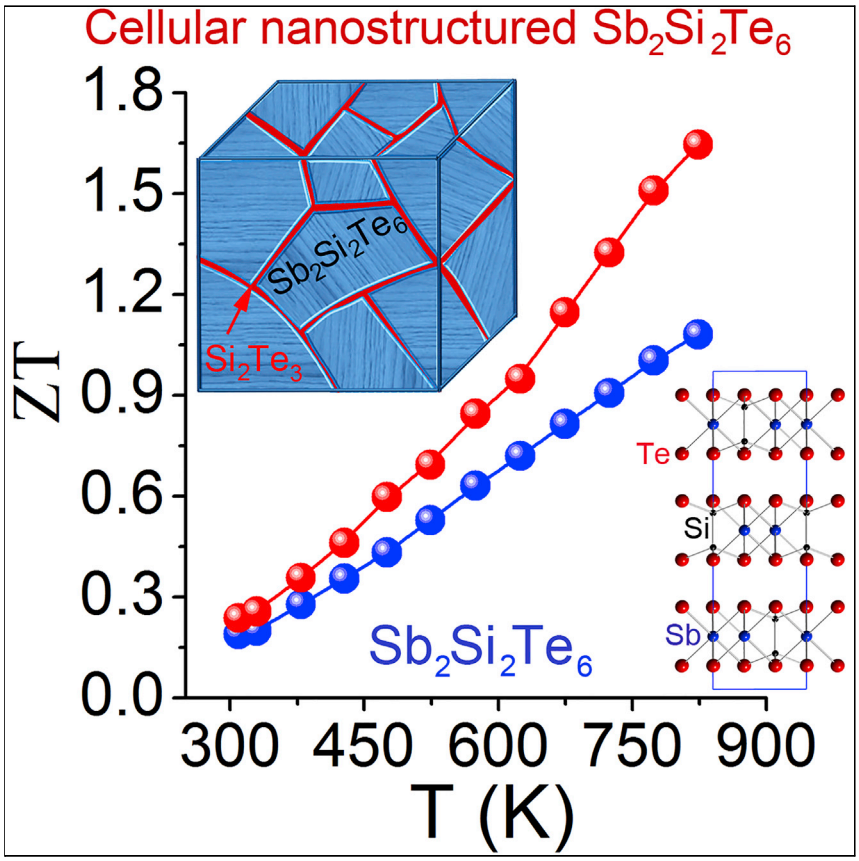

$Sb_2Si_2Te_6$, a 2D material, exhibits an intrinsically high thermoelectric figure of merit ZT of ~1.08 at 823 K. The thermoelectric performance can be further enhanced by a cellular nanostructure with ultrathin Si_2Te_3 nanosheets covering the $Sb_2Si_2Te_6$ grains. The Si_2Te_3 acts as a hole-transmitting electron-blocking filter and, at the same time, causes extra phonon scattering that leads to ultralow thermal conductivity and a high ZT value of ~1.65 at 823 K.

Yubo Luo, Songting Cai, Shiqiang Hao, ..., Arno Pfitzner, Qingyu Yan, Mercouri G. Kanatzidis

arno.pfitzner@chemie.uni-regensburg.de (A.P.)
alexyan@ntu.edu.sg (Q.Y.)
m-kanatzidis@northwestern.edu (M.G.K.)

HIGHLIGHTS

Disclosing a p-type 2D semiconductor $Sb_2Si_2Te_6$

Introducing a promising thermoelectric material system

Synthetic reaction strategy for a unique cellular nanostructure

A high ZT of ~1.65 at 823 K for the cellular nanostructured $Sb_2Si_2Te_6/Si_2Te_3$

Luo et al., Joule 4, 159–175
January 15, 2020 Published by Elsevier Inc.
https://doi.org/10.1016/j.joule.2019.10.010

Joule

CellPress

Article

High-Performance Thermoelectrics from Cellular Nanostructured $Sb_2Si_2Te_6$

Yubo Luo,[1,2] Songting Cai,[3] Shiqiang Hao,[3] Florian Pielnhofer,[4] Ido Hadar,[2] Zhong-Zhen Luo,[1,2] Jianwei Xu,[5] Chris Wolverton,[3] Vinayak P. Dravid,[3] Arno Pfitzner,[4,*] Qingyu Yan,[1,*] and Mercouri G. Kanatzidis[2,6,*]

SUMMARY

We introduce $Sb_2Si_2Te_6$ as a high-performance thermoelectric material. Single-crystal X-ray diffraction analysis indicates that $Sb_2Si_2Te_6$ has a layered two-dimensional structure with Sb^{3+} cations and $[Si_2Te_6]^{6-}$ units as building blocks adopting the $Fe_2P_2Se_6$ structure type. $Sb_2Si_2Te_6$ is a direct-band-gap semiconductor with valence-band maximum and conduction-band minimum at the Z point in the Brillouin zone, where the band is doubly degenerate. Polycrystalline bulk pellets of $Sb_2Si_2Te_6$ with randomly packed grains exhibit an intrinsically high thermoelectric figure of merit ZT of ~1.08 at 823 K. We then create a cellular nanostructure with ultrathin Si_2Te_3 nanosheets covering the $Sb_2Si_2Te_6$ grains, which act as a hole-transmitting electron-blocking filter and at the same time cause extra phonon scattering. This dual function of the cellular nanostructure achieves an ultralow thermal conductivity value of ~0.29 $Wm^{-1}K^{-1}$ and a high ZT value of ~1.65 at 823 K for $Sb_2Si_2Te_6$, along with a high average ZT value of ~0.98.

INTRODUCTION

Thermoelectric energy conversion technology using semiconductors is of broad interest because it promises to create additional efficiencies in energy management by harvesting the energy of waste heat and converting it to electrical power.[1] For this reason, there is a continuous search for new materials that can exhibit exceptionally high efficiencies. The conversion efficiency of a thermoelectric power generator is determined by the thermoelectric materials' unitless figure of merit, $ZT = S^2\sigma T/\kappa = S^2\sigma T/(\kappa_e + \kappa_L)$, where S, σ, κ, and T are the Seebeck coefficient, electrical conductivity, thermal conductivity, and absolute temperature, respectively. κ_e and κ_L are the thermal conductivity contributed by charge carriers (electrons or holes) and phonons, respectively. The S, σ, and κ_e are generally counter interrelated making it very challenging to maximize ZT.

Broad research effort worldwide has led to superior ZT values in lead antimony silver telluride (LAST) with alloying and nanoinclusions,[2] all-scale hierarchical architectures,[3] distorted electronic density of states[4] or convergent electronic band structure,[5] skutterudite with multiple-filled atom,[6] and half-Heusler with heavy band.[7] Alternatively, unusual thermoelectric single-phase compounds with peculiar behaviors have been studied, such as Cu_2Se with liquid-like behavior,[8] GeTe with low symmetry,[9] Ag_9GaSe_6 with low cutoff frequency of acoustic phonons,[10] and In_4Se_3 with Peierls distortion.[11] In particular, the recently emerging materials with 2D crystalline sheets[12–17] have shown great promise, most notably p-type[18,19] and n-type[20] single crystalline SnSe. The rapid advancement of thermoelectric materials has led to the

Context & Scale

Thermoelectric materials promise to create additional efficiencies in energy management by harvesting the energy of waste heat and converting it to electricity. We introduce 2D $Sb_2Si_2Te_6$ as a promising new high-performance thermoelectric material. $Sb_2Si_2Te_6$ exhibits an intrinsically high thermoelectric figure of merit ZT value of ~1.08 at 823 K. We then devise a unique cellular nanostructure by a post-synthetic reaction strategy that forms *in situ* Si_2Te_3 nanosheets, which serve as an effective barrier to heat propagation, yielding an ~40% reduction in the already very low lattice thermal conductivity to ~0.29 $Wm^{-1}K^{-1}$ at 823 K. The cellular nanostructure enables a very high ZT value of ~1.65 at 823 K for this new material and a high average ZT value of 0.98 (400–823 K). We describe the novel cellular nanostructure design and a single-step chemical route to achieve it, highlighting a potentially new and effective general design strategy for achieving high thermoelectric performance.

development of thermoelectric power generators. Several material systems are being explored for thermoelectric power generator prototypes such as bismuth telluride/skutterudite,[21] $Cu_2Se/Yb_{0.3}Co_4Sb_{12}$,[22] SnSe,[23] PbTe,[24] GeTe,[25] and half-Heusler[26] based thermoelectric modules.

Here, we introduce $Sb_2Si_2Te_6$, which exhibits impressive thermoelectric properties and a cellular nanostructure concept, which can be used to further optimize its performance. The crystal structure of the 2D hexatellurodisilicate compound $Sb_2Si_2Te_6$ was determined from single-crystal X-ray diffraction (XRD) data at 293 K using a crystal grown by high temperate reactions of Sb, Te, and Si_2Te_3 activated by Cl_2. We also demonstrate preparation of pure polycrystalline $Sb_2Si_2Te_6$ powders on a large scale using ball milling and annealing. The $Sb_2Si_2Te_6$, thus, can be fabricated into polycrystalline pellets using spark plasma sintering (SPS).

$Sb_2Si_2Te_6$ exhibits a doped p-type semiconductor behavior, a high Seebeck coefficient ($\sim$120 μVK^{-1} at 300 K), an intrinsically low lattice thermal conductivity ($\sim$0.5 $Wm^{-1}K^{-1}$ at 823 K), and a high ZT value of $\sim$1.08 at 823 K. Furthermore, using a post-synthetic reaction strategy (i.e., Te assisted SPS process), we form *in situ* a unique cellular network-like nanostructure with $\sim$5–20 nm ultrathin Si_2Te_3 sheets placed between the $Sb_2Si_2Te_6$ grains. The sheets of the wide-band-gap Si_2Te_3 allow good hole transmission as there is good valence band alignment between $Sb_2Si_2Te_6$ and Si_2Te_3, but act as a barrier for heat propagation, resulting in a $\sim$40% reduction in the lattice thermal conductivity to an ultralow value of $\sim$0.29 $Wm^{-1}K^{-1}$ at 823 K. This results in a peak ZT value of $\sim$1.65 at 823 K and a high average ZT of $\sim$0.98 (400–823 K) for cellular nanostructured $Sb_2Si_2Te_6/Si_2Te_3$ composite. Our work reveals the great potential of $Sb_2Si_2Te_6$ for medium-temperature thermoelectric power generation.

RESULTS AND DISCUSSION

Synthesis, Crystal Structure, Electronic Band Structure, and Microstructure

Plate-like single crystals of $Sb_2Si_2Te_6$ were obtained by reacting stoichiometric amounts of Sb, Te, and Si_2Te_3 at 873 K in an $\sim$25 kPa Cl_2 atmosphere[27] (see Experimental Procedures for details). Its crystal structure was determined by single-crystal XRD. Details of the data collection, structure solution, and refinement are given in Tables 1 and 2. Tables S1–S4 show the atomic coordinates, displacement parameters, and geometric parameters (interatomic distances, angles, and torsion angles, respectively) for $Sb_2Si_2Te_6$. The XRD crystallographic data indicate that the layered $Sb_2Si_2Te_6$ adopts rhombohedral symmetry in space group $R\bar{3}$ (No.148) and the $Fe_2P_2Se_6$ structure type, with a = 7.167 (3) Å and c = 21.186 (17) Å (Figures 1A and 1B) (the cif file of $Sb_2Si_2Te_6$ has been deposited at Cambridge Crystallographic Data Centre with a deposition number 1947640). This structure comprises stacked $Sb_2Si_2Te_6$ slabs with Sb atoms and Si-Si dumbbells ordered inside the slabs. The Sb atoms are located in the centers of Te octahedra ($SbTe_6$). The Si_2 dumbbells are also located in similar octahedral pockets forming Si_2Te_6 ethane-like groups. These $Sb_2Si_2Te_6$ slabs stack along the c axis forming van der Waals bonding in a similar fashion to Bi_2Te_3.[28] The inter-slab van der Waals Te-Te distances are $\sim$3.95 Å, in good agreement with the sum of the van der Waals radius of two Te atoms ($\sim$4.04 Å).[29] Alternatively, the $Sb_2Si_2Te_6$ can be described as a compound formed by Sb^{3+} cations and ethane-like $[Si_2Te_6]^{6-}$ anions.

Our density functional theory (DFT) electronic band structure calculations (Figure 1C) show that $Sb_2Si_2Te_6$ is a direct-gap semiconductor with both the valence-band maximum (VBM) and the conduction band minimum (CBM) located at the Z point

[1]School of Materials Science and Engineering, Nanyang Technological University, 50 Nanyang Avenue, Singapore 639798, Singapore

[2]Department of Chemistry, Northwestern University, Evanston, IL 60208, USA

[3]Department of Materials Science and Engineering, Northwestern University, Evanston, IL 60208, USA

[4]Institut für Anorganische Chemie, Universität Regensburg, Universitätsstraße 31, Regensburg 93053, Germany

[5]Institute of Materials Research and Engineering, A*STAR (Agency for Science, Technology and Research), 2 Fusionopolis Way, Innovis, Singapore 138634, Singapore

[6]Lead Contact

*Correspondence: arno.pfitzner@chemie.uni-regensburg.de (A.P.), alexyan@ntu.edu.sg (Q.Y.), m-kanatzidis@northwestern.edu (M.G.K.)

https://doi.org/10.1016/j.joule.2019.10.010

Table 1. Crystallographic Data for $Sb_2Si_2Te_6$ by Single-Crystal X-Ray Diffraction

Empirical formula	$Sb_2Si_2Te_6$
Formula weight	1,065.27 g/mol
Crystal habit	black plate
Crystal system, space group	trigonal, $R\bar{3}$
Lattice parameters: *a*	7.167(3) Å
Lattice parameters: *c*	21.186 (17) Å
Volume	942.45 (9) $Å^3$
Number of formula units, Z	3
Calculated density	5.631 g/cm^{-3}
Temperature	293 K
Wavelength	λ(Mo Kα) = 0.71073 Å
Absorption coefficient	18.09 mm^{-1}
θ range of data collection	3.3–28.3°
No. of reflections collected	1,020
Independent reflections	455
No. of refined parameters	18
No. of restraints and constraints	0, 0
$R[F^2 > 2\sigma(F^2)]$	0.017
$wR(F^2)$	0.044

$R = \sum||F_o| - |F_c||/\sum|F_o|$ $wR = \{\sum w(|F_o| - |F_c|)^2/\sum w|F_o|^2\}^{1/2}$

(0, 0, 1/2) in the Brillouin zone (Figure S1).[30] The band degeneracy of the VBM and CBM is 2 at the Z point based on the rhombohedral lattice symmetry. The doubly degenerate valence band is beneficial to high Seebeck coefficient (S), as S is proportional to density-of-states (DOS) effective mass m_d^* and $m_d^* = N_v^{2/3} m_b^*$; here, N_v and m_b^* are the band degeneracy and band effective mass of a single valley, respectably.[5] The m_b^* are ~0.26 m_0 and ~0.47 m_0 (m_0 is charge effective mass) for electrons and holes, respectively, by fitting the band structure around the CBM and VBM using $m_b^* = \hbar^2/(d^2E/dk^2)$. Accordingly, the DOS mass m_d^* are ~0.40 m_0 and 0.73 m_0 for electrons and holes, respectively. The calculated holes m_d^* is higher than p-type PbS (~0.4 m_0)[31] and PbSe (~0.28 m_0),[32] indicating a high Seebeck coefficient can also be obtained in $Sb_2Si_2Te_6$.

Considering the synthetic scalability of this material and potential thermoelectric applications, we further prepared $Sb_2Si_2Te_6$ using ball-milling and annealing processes (see Experimental Procedures for details). To characterize the phase and purity of the obtained $Sb_2Si_2Te_6$, we conducted Rietveld refinement of the powder XRD (PXRD) pattern using Fullrof program[33] (Figure 1D). It indicates that $Sb_2Si_2Te_6$ can be successfully prepared by this scalable method with a trace amount of Sb_2Te_3 (~0.6 wt %; Table S5).

Field-emission scanning electron microscopic (FESEM) imaging clearly shows that the product is made of irregularly shaped microcrystals of 1~10 μm (Figure S2). The measured optical band gap of $Sb_2Si_2Te_6$ is ~0.60 eV (Figure S3). Differential thermal analysis measurements show that $Sb_2Si_2Te_6$ is thermally stable in the temperature range of 300 K–920 K (Figure S4A) but decomposes into Sb_2Te_3 and Si_2Te_3 (red crystals) at T > 920 K (Figure S4B).

Table 2. Fractional Atomic Parameters and Equivalent Isotropic Displacement Parameters Uiso*/Ueq (Å2) for Sb2Si2Te6 at 293 K with Estimated Standard Deviations in Parentheses

	x	y	z	U_{iso}*/U_{eq}
Te1	0.33392 (3)	0.33384 (3)	0.07429 (1)	0.0166 (1)
Sb2	0	0	0.16630 (2)	0.0206 (1)
Si1	1/3	2/3	0.11261 (8)	0.0132 (3)

The polycrystalline $Sb_2Si_2Te_6$ powders were then densified using spark plasma sintering (SPS) to prepare bulk $Sb_2Si_2Te_6$ pellets. Considering the possible anisotropy that can result from the 2D nature of the structure, we studied in detail the grain orientation and microstructure. We also paid special attention to the electrical and thermal transport properties in both in-plane (perpendicular to applied pressure) and cross-plane (parallel to applied pressure) directions of the pellets (Figure S5A). Figure S5B shows the PXRD patterns taken from polished surfaces of the pellets along in- and cross-plane directions (with the scattering vector perpendicular to the flat surfaces). No obvious grain alignment could be discerned in the PXRD patterns, indicating that the pellets have a macroscopically isotropic grain-orientation distribution in the cross-sections. The arbitrarily oriented grains, observed in Figure S6, indicate a weak anisotropic character in these samples. In addition, we can see that the grains in the sintered sample show randomly oriented lamellar features with an average lateral size of 10∼30 μm. The difference in shape and size of the grains between the sintered pellet and the original powders (Figure S2) indicates a recrystallization process occurred during SPS.

Thermoelectric Properties of $Sb_2Si_2Te_6$

The essentially isotropic microstructure of the spark plasma sintered (SPSed) pellets causes almost isotropic electrical and thermal transport properties. The electrical conductivities (Figure 1E) decrease with temperature from ∼532 S/cm (in plane)/510 S/cm (cross plane) at 310 K to 163 S/cm (in plane)/160 S/cm (cross plane) at 823 K, exhibiting a heavily doped semiconductor behavior (the hole-doped character likely arises from Sb vacancies in the structure, and we discuss it below). Hall effect measurements show the $Sb_2Si_2Te_6$ has an intrinsically high hole concentration of $\sim 5.6 \times 10^{19}$ cm^{-3} at room temperature, which is in the same order of magnitude as bismuth antimony telluride[34] and Mg_2Sn.[35]

The Seebeck coefficients (Figure 1F) are consistent with the heavily doped p-type semiconductor behavior and show weak orientation dependence, which continuously increases from ∼121 μVK^{-1} (in plane)/125 μVK^{-1} (cross plane) at 310 K to ∼239 μVK^{-1} (in plane)/238 μVK^{-1} (cross plane) at 823 K. We used a single parabolic band model with acoustic phonon and point defects scattering dominant (scattering parameter $r = -1/2$)[36,37] to analyze the charge carrier transport properties. The experimental density-of-states effective mass m_d* was estimated to be ∼0.87 m_0 at room temperature, which is slightly higher than the one estimated from the calculated band structure (0.73 m_0) and may result from the higher carrier concentration and temperature in the experiment. The room temperature Seebeck coefficient (S) and m_d* of $Sb_2Si_2Te_6$ are enhanced compared to other materials with similar carrier concentrations (Table S6). For example, the values of $Sb_2Si_2Te_6$ (121 μVK^{-1}, m_d* = 0.87 m_0) are much higher than $SnCa_{0.03}Te$ (37 μVK^{-1}, m_d* = 0.28 m_0),[38] $Na_{0.005}Pb_{0.995}Se$ (37 μVK^{-1}, m_d* = 0.28 m_0),[32] and $Pb_{0.975}Na_{0.025}S$+2.0% ZnS (55 μVK^{-1}, m_d* = 0.40 m_0),[31] but are comparable to $Tl_{0.02}Pb_{0.98}Te$ (131 μVK^{-1}, m_d* = 0.91 m_0) with similar m_d*,[4] $Bi_{0.2}Sb_{1.8}Te_3$ (122 μVK^{-1}, m_d* = 0.94 m_0) with triple degenerate bands,[39] and $Pb_{0.98}Na_{0.02}Te$+6% MgTe (111 μVK^{-1}, m_d* = 1.18 m_0)[40]

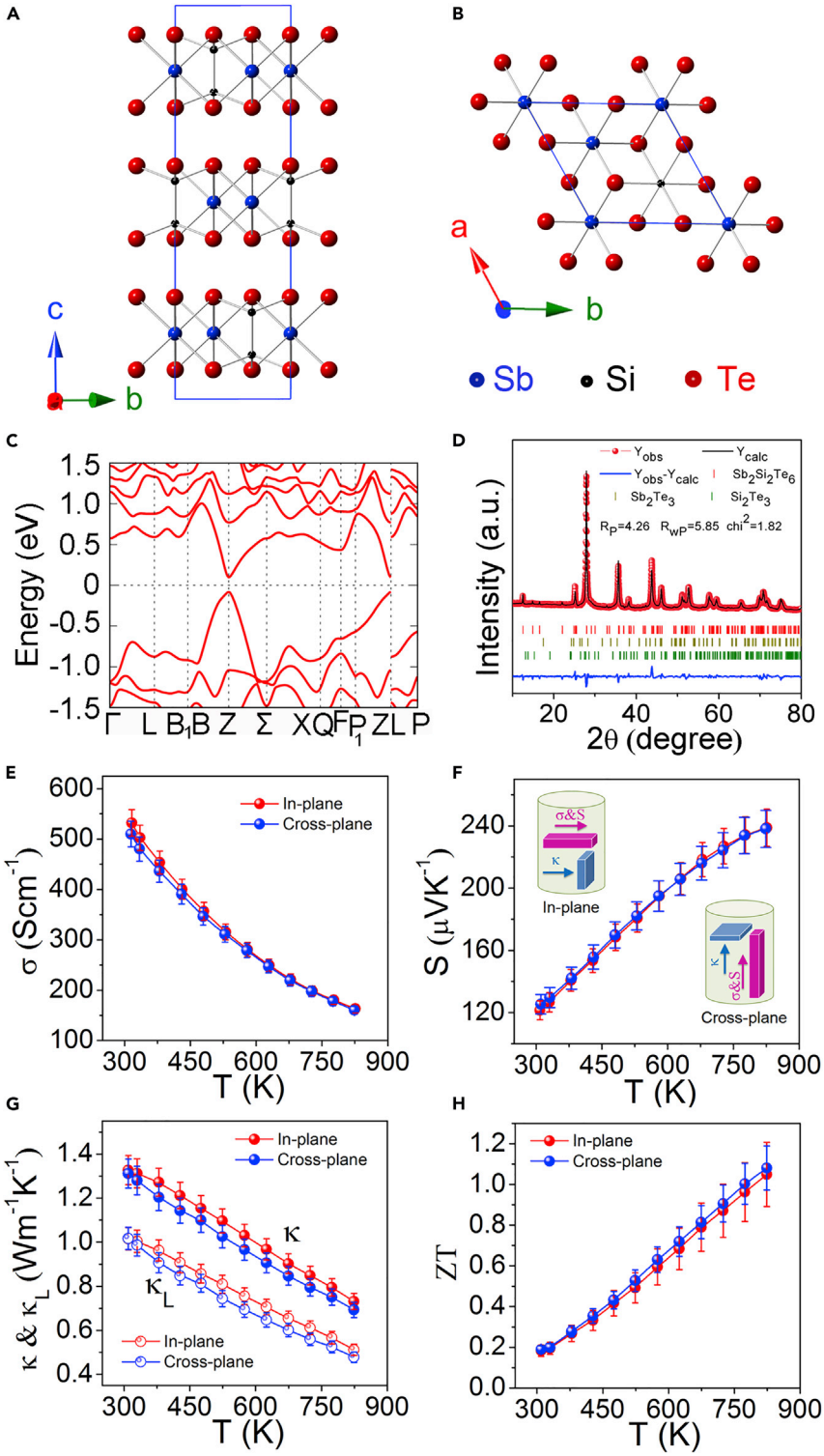

Figure 1. Crystal Structure, Density Function Theory Electronic Band Structure, Powder XRD Pattern, and Thermoelectric Properties

(A and B) Crystal structure of $Sb_2Si_2Te_6$ along the *a* axis (A) and *c* axis (B). Blue, Sb atoms; black, Si atoms; red, Te atoms. Selected distances of Sb-Te in $Sb_2Si_2Te_6$ are 3.0864(4) Å and 3.0913(4) Å.

Figure 1. *Continued*
(C) Electronic band structure of $Sb_2Si_2Te_6$ indicates a parabolic band configuration and a direct band gap.
(D) Rietveld refinement of the powder XRD pattern of $Sb_2Si_2Te_6$.
(E–H) Temperature-dependent (E) electrical conductivities, (F) Seebeck coefficients, (G) thermal conductivities, and (H) figure of merits ZT of $Sb_2Si_2Te_6$ pellet.

with convergent valence bands. Therefore, the high hole effective mass and doubly degenerate bands at the Z point for $Sb_2Si_2Te_6$ are beneficial to the Seebeck coefficient.

The in-plane thermal conductivities in SPSed $Sb_2Si_2Te_6$ samples (Figure 1G) are low and decrease from ~1.33 $Wm^{-1}K^{-1}$ at 310 K to ~0.74 $Wm^{-1}K^{-1}$ at 823 K, and the cross-plane ones decrease from ~1.26 $Wm^{-1}K^{-1}$ at 310 K to ~0.69 $Wm^{-1}K^{-1}$ at 823 K. The cross-plane thermal conductivity values are about 93%–96% of the in-plane thermal conductivities in the temperature range of 310 K–823 K (Figure S7A). The lattice thermal conductivities κ_L, obtained by subtracting the electronic thermal conductivities (Figure S7B) are shown in Figure 1G. The in- and cross-plane κ_L values are also almost isotropic with a difference of less than 9% (Figure S7C) in the temperature interval of 310 K–823 K and decrease from ~1.0 $Wm^{-1}K^{-1}$ at 310 K to ~0.5 $Wm^{-1}K^{-1}$ at 823 K.

The in- and cross-plane ZT values are approximately isotropic as a result of the weak orientation related electrical and thermal transport properties (Figure 1H). It is noted that the cross-plane ZT values rise from ~0.19 at 310 K to ~1.08 at 823 K. This value is much higher than that of its isostructural materials $Cr_2Ge_2Te_6$[41] and $In_2Ge_2Te_6$.[42]

Native Point Defects and Phonon Propagation in $Sb_2Si_2Te_6$

We performed DFT calculations to better understand the native defects and phonon propagation physics of $Sb_2Si_2Te_6$. Figures 2A and 2B present the Fermi level-dependent formation energy of various possible negatively charged point defects (V_{Sb}, V_{Si}, Sb_{Te}, and Si_{Te}) in Te- and Sb-rich environments, respectively. The defect formation energies are evaluated as[43]

$$E_{form} = E_d - E_p + \sum n_i\mu_i + q(\Delta E_F + E_{VBM}), \qquad \text{(Equation 1)}$$

where E_d and E_p are the total energies for defective and defect free supercells, n_i and μ_i are the number of atoms being removed or added and the corresponding chemical potential, q is the charge state of the defect, and ΔE_F and E_{VBM} are the Fermi energy and energy levels corresponding to the VBM, respectively.

We can see that the formation energy of Sb vacancy (V_{Sb}^{3-}) is always negative and much lower than other possible point defects. This indicates that Sb vacancies are the most stable native acceptor defects. They are easy to form and act as the dominant native point defects in $Sb_2Si_2Te_6$, leading to the high hole concentration in $Sb_2Si_2Te_6$.

Figure 2C shows the phonon dispersion spectrum of $Sb_2Si_2Te_6$. There is no imaginary frequency to be found in the whole Brillouin zone, confirming the $Sb_2Si_2Te_6$ structure as determined by our single crystal study is kinetically stable. The TA′ and LA modes show a normal linear dispersion around the Γ-point, while the TA mode (atomic motions along c axis) shows a quadratic energy dispersion relation in frequency near the Γ point. We attribute the quadratic energy dispersion relation to the point-group symmetry of the layered $Sb_2Si_2Te_6$, as observed in other 2D systems.[44,45]

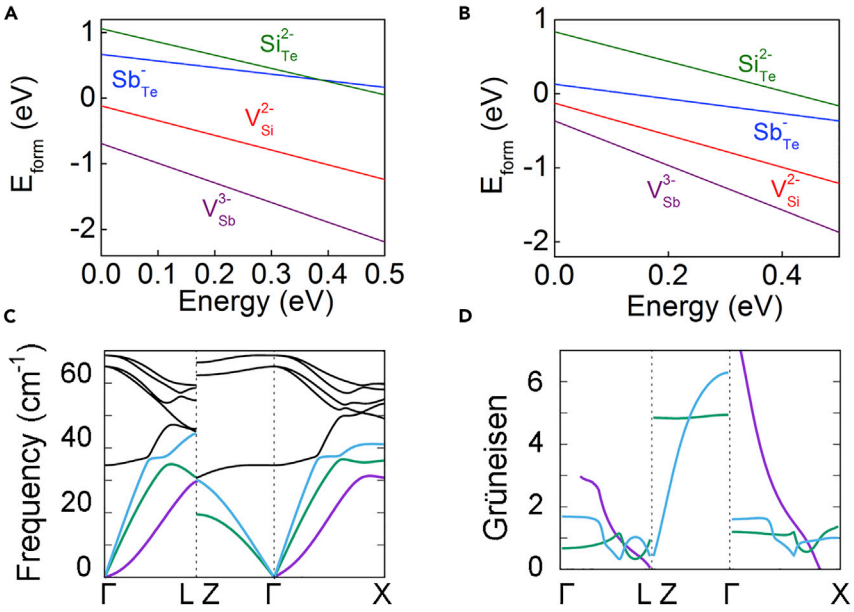

Figure 2. DFT Calculations of the Native Defect and Phonon Propagation Physics in $Sb_2Si_2Te_6$

Fermi level-dependent defect formation energies for charged isolated point defects under (A) Te-rich and (B) Sb-rich conditions, (C) phonon dispersive curves, and (D) Grüneisen dispersions of $Sb_2Si_2Te_6$. The transverse acoustic (TA and TA′) modes and the longitudinal acoustic (LA) mode are colored by purple, green, and light blue, respectively in the phonon spectra (C). Similarly, the Grüneisen dispersions from TA, TA′, and LA are colored by purple, green, and light blue in (D).

The maximum frequency of acoustic phonon modes in $Sb_2Si_2Te_6$ is ~44 cm^{-1}, which is even lower than that of the well-known benchmark material SnSe (~50 cm^{-1})[16] and Sb_2Te_3 (~60 cm^{-1}).[46] In addition, there are some low-frequency transverse optical phonon modes gathered in the acoustic region (below ~44 cm^{-1}). Atomic projected density of state analysis (Figure S8) suggests the low-frequency optical modes mainly result from the low-frequency vibrations of Sb and Te atoms, indicated by the peaks at ~35 cm^{-1}. This interaction implies a coupling between the optical phonon modes and acoustic phonon modes, which would enhance acoustic scattering, reduce the phonon relaxation time and shorten the phonon mean free path.

Moreover, the phonon frequency shows a significant anisotropy along different directions of the Brillouin zone consistent with the strongly 2D crystal structure. For instance, the TA, TA′, and LA modes along the Γ–Z direction (interlayer) are much softer than that along Γ–L and Γ–X directions, in good agreement with the weaker van der Waals interlayer bonding.

Typical dispersions of the Grüneisen parameters γ of the acoustic modes are shown in Figure 2D. The γ values are high for the TA, TA′, and LA modes along these directions, with average values estimated to be 0.91, 1.85, and 4.81 along the Γ–L, Γ–X, and Γ–Z directions, respectively. The high Grüneisen parameters along the Γ–Z direction imply a strong phonon anharmonicity in $Sb_2Si_2Te_6$, which would strongly influence the phonon–phonon Umklapp process, thereby limiting the lattice thermal conductivity.

The phonon group velocity of each mode is given by $\nu_g = d\omega/d\kappa$, where ω and κ represent the vibrational frequency and wave vector, respectively.[47] The phonon

velocities are 1,250, 1,810, and 2,450 m/s for TA, TA′, and LA, respectively. The averaged sound velocity is about 2,080 m/s, which is much lower than typical solid-state materials (~3,000 m/s) and comparable to other well-established thermoelectric materials (e.g., SnTe, PbTe, and PbSe).[48] Therefore, the low phonon group velocity, optical, and acoustic phonon coupling along with the anharmonic phonon scattering should be the origin of the intrinsically low lattice thermal conductivity in $Sb_2Si_2Te_6$.

Formation of Cellular Nanostructured $Sb_2Si_2Te_6$

Previous theoretical simulations[49,50] and experimental studies[51–53] have shown that nanoscale shells can significantly suppress heat propagation within materials, even in low thermal conductivity materials. However, such unique nanostructures are not trivial to create because suitable direct chemical routes are lacking. Often, they can be achieved by wet chemical approaches involving nanoparticles,[51–53] which are difficult to scale up for practical applications. In $Sb_2Si_2Te_6$, we have found a straightforward post-synthetic reaction strategy to easily create a cellular nanostructure wherein, the cellular network walls are made of Si_2Te_3 second phase. This was achieved by decomposing a small fraction of $Sb_2Si_2Te_6$ in liquid Te (e.g., 10 wt %) at high temperature (Figure S9), as

$$Sb_2Si_2Te_6 \rightarrow Sb_2Te_3 + Si_2Te_3. \qquad \text{(Equation 2)}$$

This reaction develops ultrathin Si_2Te_3 sheets forming a network acting as the cell walls on $Sb_2Si_2Te_6$ grains acting as the cells. This happens on the crystal edges and creates the products Sb_2Te_3 and Si_2Te_3. Most of the reaction products dissolve in liquid Te and are squeezed out of the pellets during the SPS process (hereinafter referred to as Te processed) (Figures S10 and S11), leaving behind a 3D network of thin nanosheets of Si_2Te_3 covering the $Sb_2Si_2Te_6$ grains as we show below.

The Rietveld refinement of the PXRD pattern (Figure S12) shows that in the Te-processed sample the weight fractions of residual Sb_2Te_3 and Si_2Te_3 are ~2.4 and ~1.3 wt %, respectively (Table S5). In addition, backscattered electron (BSE) images (Figure S13) show that the residual Sb_2Te_3 tends to aggregate forming mesoscale grains, which shows weak influence on the thermoelectric performance of $Sb_2Si_2Te_6$ (Figure S14). FESEM images (Figure S15) of the fractured cross-section of the Te-processed samples indicate that there is no apparent difference in the polycrystalline microstructure (e.g., grains' geometry and arrangement) of the sintered samples compared to pristine $Sb_2Si_2Te_6$ (Figure S6).

The samples resulting from this process were examined with scanning/transmission electron microscopy (S/TEM) with energy dispersive spectroscopy (STEM-EDS) to investigate the interfaces at the $Sb_2Si_2Te_6$ grains. Figure 3 shows such images from the 10 wt % Te-processed sample (10 Te). Mesoscale $Sb_2Si_2Te_6$ crystallites (Figure 3A) with multiple crystallographic orientations (e.g., [031], [010]) can be readily observed from the high-resolution TEM images and the selected area electron diffraction (SAED) patterns (Figures 3B–3E). In addition, the samples exhibit dense intragranular dislocations (Figure 3F) with an areal dislocation density of ~6×10^{10} cm^2. This dislocation density is likely an underestimation given the presence of invisible dislocations caused by extinction and orientation.[54] In general, dense dislocations are commonly observed in thermoelectric materials prepared by a similar liquid-phase compaction method,[55] but they are mainly concentrated in grain boundaries. Therefore, the observed dense intragranular dislocations are formed in a different way, and are attributed to the high Sb vacancy concentration in $Sb_2Si_2Te_6$, since the pristine $Sb_2Si_2Te_6$ itself also shows dense intragranular dislocations (Figure S16).

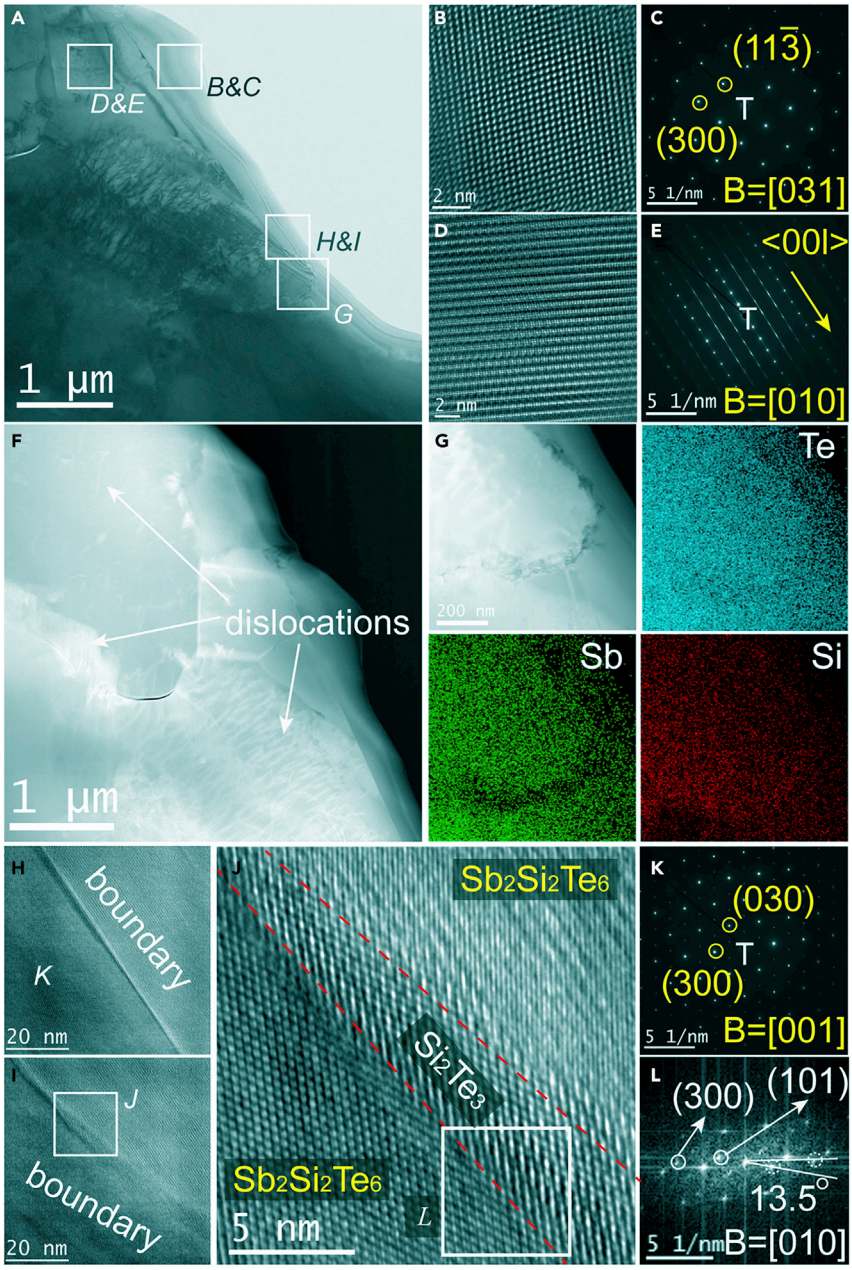

Figure 3. Scanning/Transmission Electron Microscopic Characterizations of 10 Te Sample

(A–C) Low magnified TEM (A), high-resolution TEM (B), and selected area electron diffraction (SAED) (C) pattern taken along [031].

(D and E) High-resolution TEM (D) and SAED pattern (E) taken along [010].

(F) High-angle annular dark-field (HAADF) image.

(G) Corresponding energy dispersive spectroscopic (EDS) elemental mapping.

(H–J) Low magnified TEM (H and I) and high-resolution TEM (J) of the grain boundary.

(K and L) SAED pattern of the area marked in (H) (K) and fast Fourier transformation (FFT) pattern of the boundary marked in (J) (L).

High-angle annular dark-field scanning transmission electron microscopic (HAADF-STEM) images, which are sensitive to chemical composition, show a sharp dark contrast region at the grain boundary (Figure 3G). The dark region arises from the lowest atomic number and should be Si rich. In addition, the corresponding

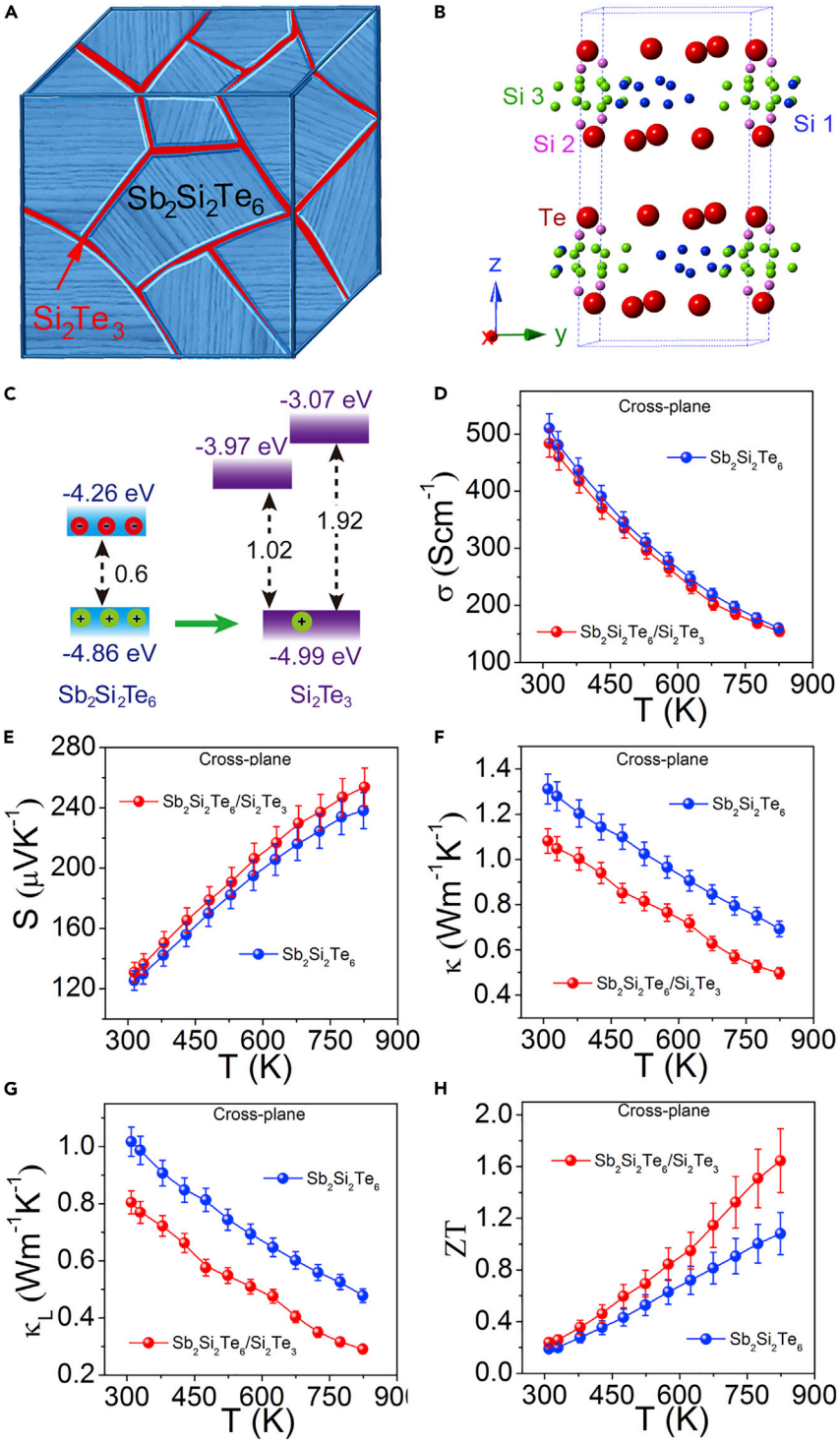

Figure 4. Cellular Nanostructured $Sb_2Si_2Te_6/Si_2Te_3$, Crystal Structure of Si_2Te_3, Band Alignment, and Thermoelectric Properties

(A and B) Schematic illustration of the cellular nanostructure (A) and crystal structure of Si_2Te_3 (B). Silicon occupancies of Si1, Si2, and Si3 are 1/3, 1/2, and 1/6, respectively.

(C) Schematic illustration of band alignment.

Figure 4. *Continued*
(D–H) The temperature-dependent cross-plane (D) electrical conductivities, (E) Seebeck coefficients, (F) thermal conductivities, (G) lattice thermal conductivities, and (H) ZT values for pristine $Sb_2Si_2Te_6$ and cellular nanostructured $Sb_2Si_2Te_6/Si_2Te_3$ processed by 10 wt % Te (10 Te), respectively.

STEM-EDS elemental mapping characterization indicates the dark region is Si rich but Sb poor. The thickness of the dark region is estimated to be ~5–20 nm (Figures 3G–3I). Furthermore, the clear lattice fringes in the lattice resolved high-resolution transmission electron microscopy (HRTEM) image (Figure 3J), corresponding SAED (Figure 3K), and fast Fourier transform (FFT) dots (Figure 3L) demonstrate that the dark region is composed by highly crystalline Si_2Te_3. The FFT dots belong to α-Si_2Te_3 (white) and derive from the (300) and (101) planes with an angle of 13.5°, which implies an axis zone compatible with the [010] direction of Si_2Te_3.

Band Alignment and Thermoelectric Properties of Cellular Nanostructured $Sb_2Si_2Te_6/Si_2Te_3$

The above microstructure characterization confirms the formation of cellular nanostructured $Sb_2Si_2Te_6/Si_2Te_3$ nanocomposite (Figure 4A) by the post-synthetic reaction route. The second phase Si_2Te_3 is also a 2D van der Waals semiconductor and crystallizes in the trigonal space group $P\bar{3}1c$, with a = 7.430 (5) Å and c = 13.482 (7) Å[56] (Figure 4B). Each layer consists of two planes of hexagonally close-packed Te atoms, and orientational Si-Si dumbbells, which occupy 2/3 of the octahedral sites defined the Te planes. It is noted that there are 28 possible positions in hexagonal close-packed Te sublattice for eight Si atoms, thus the occupancy of Si sites and the orientation of Si dumbbells are spread over these positions. The special 2D and disordered structure of Si_2Te_3 leads to an intrinsically low thermal conductivity of ~0.4–0.5 $Wm^{-1}K^{-1}$ at room temperature.[57]

The cellular nature of the nanostructure is composed of narrow band-gap majority phase $Sb_2Si_2Te_6$ separated by the thin sections of the wide band-gap minority phase Si_2Te_3. This arrangement has a favorable band alignment between the two phases in which the valence band tops are close in energy allowing holes (majority carriers) to transfer across but the conduction band bottoms are very different in energy thereby creating a barrier for electrons (minority carriers).

The VBM energies (Ev) for $Sb_2Si_2Te_6$ and Si_2Te_3, using photoemission yield spectroscopy in air (PYSA) (Figure S17), are −4.99 and −4.86 eV, respectively. The energy diagram is schematically shown in Figure 4C. The PYSA measurements[58] were performed on pure samples of $Sb_2Si_2Te_6$ and Si_2Te_3 (Figure S18) and described in the Supplemental Information. The energy difference of the valence bands at room temperature between $Sb_2Si_2Te_6$ and Si_2Te_3 is only ~0.13 eV, which is low enough to have negligible effect on the transmission of holes across the $Sb_2Si_2Te_6/Si_2Te_3$ interface.[59,60] We further estimated the CBM energies (E_c) of $Sb_2Si_2Te_6$ and Si_2Te_3 using $E_c = E_v + E_g$, where the Si_2Te_3 has an indirect band gap of ~1.02 eV and a direct band gap of ~1.92 eV (Figure S3B). The energy difference of the conduction bands is ~0.29 eV (indirect band) and ~1.19 eV (direct band) between $Sb_2Si_2Te_6$ and Si_2Te_3 (Figure 4C). The high conduction band offset indicates that Si_2Te_3 could block the flow of electrons between $Sb_2Si_2Te_6$ grains, which is expected to enhance the net Seebeck coefficient.[61,62]

Figures 4D–4H show the cross-plane thermoelectric properties of pristine $Sb_2Si_2Te_6$ and cellular nanostructured $Sb_2Si_2Te_6/Si_2Te_3$. The presence of the hole-transmitting

electron-blocking filter (Si_2Te_3) created by the favorable valence band alignment has a small effect on the carrier concentrations and mobilities which change from 5.46 × 10^{19} cm^{-3}, ~58 $cm^2V^{-1}S^{-1}$ in pristine $Sb_2Si_2Te_6$ to 5.28 × 10^{19} cm^{-3}, ~57 $cm^2V^{-1}S^{-1}$ in $Sb_2Si_2Te_6/Si_2Te_3$ (10 Te; Table S7), which leads to a small conductivity decrease from ~510 S/cm to ~483 S/cm at room temperature (Figure 4D), and a small Seebeck coefficients increase from ~238.1 μVK^{-1} in $Sb_2Si_2Te_6$ to ~253.8 μVK^{-1} in $Sb_2Si_2Te_6/Si_2Te_3$ at ~823 K. As a result, the power factor $S^2\sigma$ of $Sb_2Si_2Te_6/Si_2Te_3$ is slightly higher than pure $Sb_2Si_2Te_6$ in the whole measurement temperature range of 310–823 K (Figure S19).

Another important property of the cellular nanostructure is its lower thermal conductivity (Figure 4F). The thermal conductivity of $Sb_2Si_2Te_6/Si_2Te_3$ is ~0.50 $Wm^{-1}K^{-1}$ at 823 K, which is ~28% lower than that of $Sb_2Si_2Te_6$ at 823 K, respectively. This is mainly ascribed to the large drops in lattice thermal conductivities (Figure 4G). For instance, the lattice thermal conductivity of $Sb_2Si_2Te_6/Si_2Te_3$ drops to only ~0.29 $Wm^{-1}K^{-1}$ at 823 K, which is ~40% less than the value (~0.48 $Wm^{-1}K^{-1}$) of $Sb_2Si_2Te_6$ at 823 K. We attribute the large reduction in the lattice thermal conductivity to the extra scattering of phonons by the nanoscale Si_2Te_3 sheets.

The large reduction in thermal conductivity achieves a peak ZT of ~1.65 at 823 K in the cellular nanostructured $Sb_2Si_2Te_6/Si_2Te_3$ (Figure 4H). The average ZT values (400–823 K) of $Sb_2Si_2Te_6$ and $Sb_2Si_2Te_6/Si_2Te_3$ are ~0.66 and ~0.98, an increase of ~48% (Figure S20). Such a high ZT_{avg} value is comparable to other optimized environmentally friendly thermoelectric materials (e.g., SnSe[63] and BiCuSeO[64]), making the cellular nanostructured $Sb_2Si_2Te_6/Si_2Te_3$ competitive for heat to electricity conversion device applications. More importantly, the cellular nanostructured $Sb_2Si_2Te_6/Si_2Te_3$ exhibits high thermal stability in microstructure (Figures S21 and S22) and thermoelectric performance (Figures S23 and S24). The ZT values did not vary by more than 5% even after 6 thermal cycles. Also, we estimated the phase components of cellular nanostructured $Sb_2Si_2Te_6/Si_2Te_3$ after 6 thermal cycles (Figure S25) by the Rietveld refinement. The weight fractions of Sb_2Te_3 and Si_2Te_3 are ~3.1 wt % and ~1.7 wt %, respectively (Table S6), which are slightly higher than that of as-prepared one.

Thermoelectric Properties of Cellular Nanostructured $Sb_2Si_2Te_6/Si_2Te_3$ Composites as a Function of Te Amount

Figure 5 depicts the thermoelectric properties of cellular nanostructured $Sb_2Si_2Te_6/Si_2Te_3$ created with different Te amounts (i.e., 5 wt %, 10 wt %, and 15 wt %). Considering the possible grain alignment promoted by liquid Te,[65] the thermoelectric properties were measured along both in- and cross-plane directions of the pellets. Like the pristine $Sb_2Si_2Te_6$, the in- and cross-plane thermoelectric properties are also nearly isotropic in these samples, indicating Te processing does not lead to a substantial change in grain orientation.

The electrical transport properties of cellular nanostructured $Sb_2Si_2Te_6/Si_2Te_3$ samples created with 5 wt % Te (5 Te), 10 wt % Te (10 Te), and 15 wt % Te (15 Te) processed samples are similar. For example, the cross-plane electrical conductivities (Figure 5A) and Seebeck coefficients (Figure 5B) at ~823 K are ~157 S/cm and ~255.0 μVK^{-1}, ~154 S/cm and ~253.8 μVK^{-1}, and ~148 S/cm and ~260.7 μVK^{-1} for 5 Te, 10 Te, and 15 Te, respectively. These values result in similar power factors in these samples (Figure 5C). In addition, only small differences in the thermal transport properties were observed. For example, the cross-plane thermal conductivities

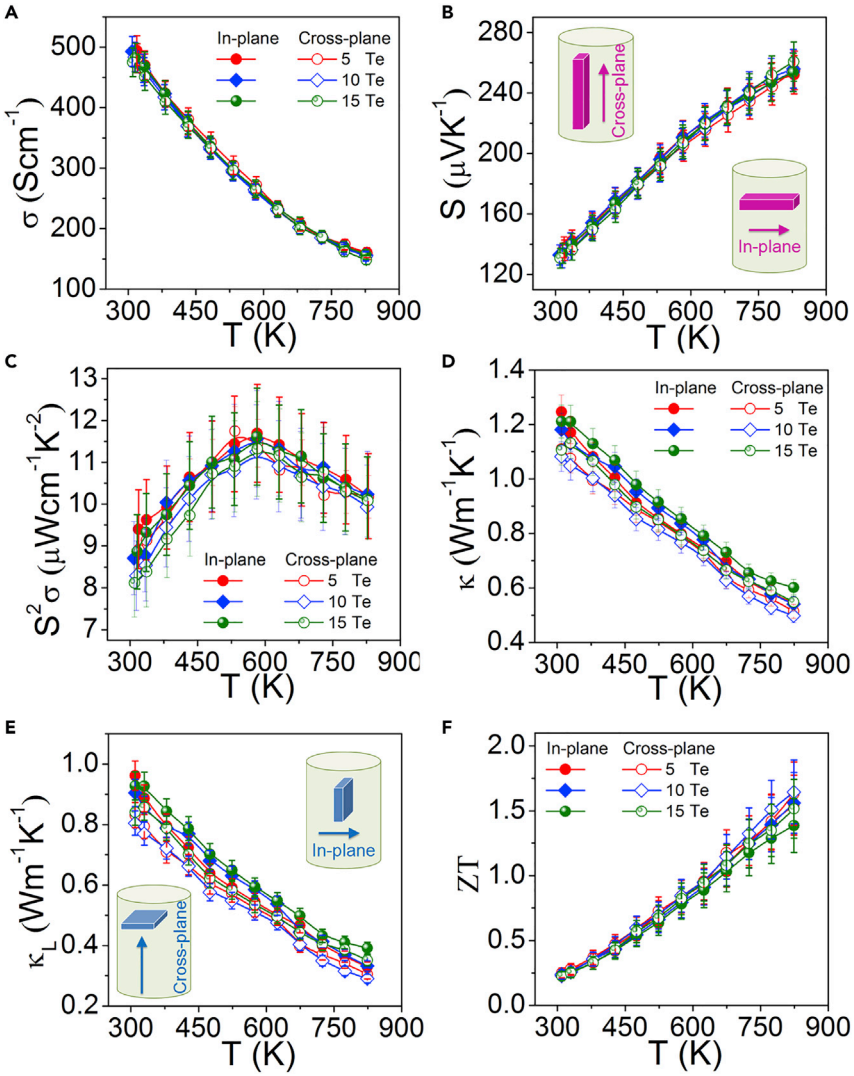

Figure 5. Thermoelectric Properties of Cellular Nanostructured $Sb_2Si_2Te_6/Si_2Te_3$ Samples Created with Different Te Amounts

Temperature-dependent in- and cross-plane (A) electrical conductivities, (B) Seebeck coefficients, (C) power factors, (D) thermal conductivities, (E) lattice thermal conductivities, and (F) ZT values for $Sb_2Si_2Te_6/Si_2Te_3$ samples created with 5 wt % Te (5 Te), 10 wt % Te (10 Te), and 15 wt % Te (15 Te).

(at ~823 K) are ~0.51 $Wm^{-1}K^{-1}$, ~0.50 $Wm^{-1}K^{-1}$ and ~0.55 $Wm^{-1}K^{-1}$ for 5 Te, 10 Te, and 15 Te, respectively (Figure 5D), while the lattice thermal conductivities (at ~823 K) are ~0.30 $Wm^{-1}K^{-1}$, ~0.29 $Wm^{-1}K^{-1}$ and ~0.35 $Wm^{-1}K^{-1}$, respectively (Figure 5E).

The peak ZT values (at 823 K) for 5 Te, 10 Te, and 15 Te are 1.54, 1.56, and 1.39 along in-plane direction and 1.63, 1.65, and 1.51 along cross-plane direction, respectively (Figure 5F). These results show that Te amount has a small effect on the thermoelectric performance of $Sb_2Si_2Te_6$, because most of the reaction products (Sb_2Te_3 and Si_2Te_3) dissolved in liquid Te and were squeezed out during SPS.

We have revealed a chemical route to a unique cellular nanostructured $Sb_2Si_2Te_6/Si_2Te_3$ that is a new promising p-type high performance thermoelectric material,

although its large-scale application may be limited by the relative scarcity of tellurium. The ultrathin Si_2Te_3 effectively blocks the transmission of electrons while negligibly affects the transmission of holes between $Sb_2Si_2Te_6$ grains, because of the well matching valence band energies between $Sb_2Si_2Te_6$ and Si_2Te_3. Therefore, such cellular nanostructure enables concurrent higher power factor and lower thermal conductivity from 310 and 823 K, and reaches a ZT value of ~1.65 at 823 K with a high average ZT value of ~0.98 (400–823 K). This suggests great potential for practical thermoelectric applications at medium temperatures. The cellular network nanostructure design highlights a novel, general, and effective strategy for achieving high thermoelectric performance from already excellent thermoelectric materials, provided a viable single-step chemical route can be devised to achieve it.

EXPERIMENTAL PROCEDURES

Synthesis of Single Crystals of $Sb_2Si_2Te_6$

Si_2Te_3 was prepared by a stoichiometric reaction of Si wafers (99.999%) and Te (99.999%) at 1,173 K in evacuated quartz ampoules. Then, stoichiometric starting materials Sb, Te, and Si_2Te_3 (2:3:1) and a small amount of $CrCl_3$ were mixed, evacuated, and sealed in quartz ampoules. $CrCl_3$ was used as Cl_2 source to activate Si, because $CrCl_3$ decomposes at 873K:

$$CrCl_3 \xrightarrow{873K} CrCl_2 + \frac{1}{2}Cl_2. \qquad \text{(Equation 3)}$$

The pressure of Cl_2 was estimated using the assumption of an ideal gas PV = nRT and controlled at 25 KPa (873 K) for the synthesis of single crystalline $Sb_2Si_2Te_6$. In which, P and V are the pressure and volume of Cl_2 gas, n is the number of moles of Cl_2 gas, R is the ideal gas constant, and T is the absolute temperature. The mixtures were slowly heated to 873 K and kept there for 2 months. Besides the $Sb_2Si_2Te_6$, a small amount of Sb_2Te_3 byproduct was also observed.[18]

Synthesis of Polycrystalline $Sb_2Si_2Te_6$

Polycrystalline pure phase of $Sb_2Si_2Te_6$ was synthesized by ball milling and annealing processes. High-purity Sb shots (99.9999%, American Elements), Si powders (99.999%, 5N Plus, Alfa Aesar), Te shots (99.999%, American Elements), and stearic acid (98.5%, Sigma Aldrich) were used as the starting materials. Stoichiometric starting materials Sb (1.82625 g), Si (0.42128 g), Te (5.742 g), and stearic acid (5 mg) were loaded into a stainless-steel jar (50 mL) with 7 stainless-steel balls (diameter 10 mm). Inside a glove box the jar was evacuated, N_2-filled, and sealed. The jar was then taken outside of the glove box and subjected to a planetary ball mill (PM 100, RETSCH) with a rotational speed of 450 rpm for 2 h. The obtained powder sample (Figure S26) was taken in the glove box and loaded into 13 mm diameter silica tubes and then flame-sealed under a residual pressure of $\sim 10^{-4}$ Torr. The tube was vertically placed in a box furnace, slowly heated to 823 K for 5 h, annealed at this temperature for 2 days, and finally cooled to room temperature naturally.

SUPPLEMENTAL INFORMATION

Supplemental Information can be found online at https://doi.org/10.1016/j.joule.2019.10.010.

ACKNOWLEDGMENTS

We acknowledge the support from the Department of Energy, Office of Science Basic Energy Sciences under grant DE-SC0014520, DOE Office of Science (sample preparation, synthesis, XRD, TE measurements, TEM measurements, and DFT

calculations, Northwestern University), and from the Deutsche Forschungsgemeinschaft DFG in the framework of SPP 1666 under grant PF 324/4-1 (AP). This work made use of the EPIC facilities of Northwestern's NUANCE Center, which has received support from the Soft and Hybrid Nanotechnology Experimental (SHyNE) Resource (NSF ECCS-1542205); the MRSEC program (NSF DMR-1720139) at the Materials Research Center; the International Institute for Nanotechnology (IIN); the Keck Foundation; and the State of Illinois, through the IIN. User Facilities are supported by the Office of Science of the U.S. Department of Energy under contract no. DE-AC02-06CH11357 and DE-AC02-05CH11231 and the ONR funding-PYSA measurements (ONR grant N00014-18-1-2102). Access to facilities of high-performance computational resources at the Northwestern University is acknowledged. The authors also acknowledge National Natural Science Foundation of China (61728401), Singapore MOE AcRF Tier 2 under grant nos. 2018-T2-1-010 and 2017-T2-2-069, Singapore A*STAR Pharos Program SERC 1527200021 and 1527200022, and the support from FACTs of Nanyang Technological University for sample analysis.

AUTHOR CONTRIBUTIONS

Y.L., Q.Y.Y., and M.G.K. conceived and designed the experiments; Y.L., Z.-Z.L., and I.H. synthesized polycrystalline samples and characterized their properties; S.C. and V.P.D. collected TEM data; S.H. and C.W. performed DFT calculations; F.P. and A.P. synthesized single crystalline samples; J.X. performed the discussion; and all authors wrote and revised the manuscript.

DECLARATION OF INTERESTS

The authors declare no competing interests.

Received: August 16, 2019
Revised: September 21, 2019
Accepted: October 22, 2019
Published: November 19, 2019

REFERENCES

1. He, J., and Tritt, T.M. (2017). Advances in thermoelectric materials research: looking back and moving forward. Science *357*, 1369.
2. Hsu, K.F., Loo, S., Guo, F., Chen, W., Dyck, J.S., Uher, C., Hogan, T., Polychroniadis, E.K., and Kanatzidis, M.G. (2004). Cubic $AgPb_mSbTe_{2+m}$: bulk thermoelectric materials with high figure of merit. Science *303*, 818–821.
3. Biswas, K., He, J., Blum, I.D., Wu, C.I., Hogan, T.P., Seidman, D.N., Dravid, V.P., and Kanatzidis, M.G. (2012). High-performance bulk thermoelectrics with all-scale hierarchical architectures. Nature *489*, 414–418.
4. Heremans, J.P., Jovovic, V., Toberer, E.S., Saramat, A., Kurosaki, K., Charoenphakdee, A., Yamanaka, S., and Snyder, G.J. (2008). Enhancement of thermoelectric efficiency in PbTe by distortion of the electronic density of states. Science *321*, 554–557.
5. Pei, Y., Shi, X., LaLonde, A., Wang, H., Chen, L., and Snyder, G.J. (2011). Convergence of electronic bands for high performance bulk thermoelectrics. Nature *473*, 66–69.
6. Shi, X., Yang, J., Salvador, J.R., Chi, M., Cho, J.Y., Wang, H., Bai, S., Yang, J., Zhang, W., and Chen, L. (2011). Multiple-filled skutterudites: high thermoelectric figure of merit through separately optimizing electrical and thermal transports. J. Am. Chem. Soc. *133*, 7837–7846.
7. Zhu, H., He, R., Mao, J., Zhu, Q., Li, C., Sun, J., Ren, W., Wang, Y., Liu, Z., Tang, Z., et al. (2018). Discovery of ZrCoBi based half Heuslers with high thermoelectric conversion efficiency. Nat. Commun *9*, 2497.
8. Liu, H., Shi, X., Xu, F., Zhang, L., Zhang, W., Chen, L., Li, Q., Uher, C., Day, T., and Snyder, G.J. (2012). Copper ion liquid-like thermoelectrics. Nat. Mater *11*, 422–425.
9. Li, J., Zhang, X., Chen, Z., Lin, S., Li, W., Shen, J., Witting, I.T., Faghaninia, A., Chen, Y., Jain, A., et al. (2018). Low-symmetry rhombohedral GeTe thermoelectrics. Joule *2*, 976–987.
10. Lin, S., Li, W., Li, S., Zhang, X., Chen, Z., Xu, Y., Chen, Y., and Pei, Y. (2017). High thermoelectric performance of Ag_9GaSe_6 enabled by low cutoff frequency of acoustic phonons. Joule *1*, 816–830.
11. Rhyee, J.S., Lee, K.H., Lee, S.M., Cho, E., Kim, S.I., Lee, E., Kwon, Y.S., Shim, J.H., and Kotliar, G. (2009). Peierls distortion as a route to high thermoelectric performance in $In_4Se_{3-\delta}$ crystals. Nature *459*, 965–968.
12. Chung, D.Y., Hogan, T., Brazis, P., Rocci-Lane, M., Kannewurf, C., Bastea, M., Uher, C., and Kanatzidis, M.G. (2000). $CsBi_4Te_6$: a high-performance thermoelectric material for low-temperature applications. Science *287*, 1024–1027.
13. Zhou, Y., and Zhao, L.D. (2017). Promising thermoelectric bulk materials with 2D structures. Adv. Mater *29*, 28737228.
14. Luo, Y., Zheng, Y., Luo, Z., Hao, S., Du, C., Liang, Q., Li, Z., Khor, K.A., Hippalgaonkar, K., Xu, J., et al. (2018). n-type $SnSe_2$ oriented-nanoplate-based pellets for high thermoelectric performance. Adv. Energy Mater *8*, 1702167.
15. Ohno, S., Imasato, K., Anand, S., Tamaki, H., Kang, S.D., Gorai, P., Sato, H.K., Toberer, E.S., Kanno, T., and Snyder, G.J. (2018). Phase boundary mapping to obtain n-type Mg_3Sb_2 based thermoelectrics. Joule *2*, 141–154.
16. Li, B., Wang, H., Kawakita, Y., Zhang, Q., Feygenson, M., Yu, H.L., Wu, D., Ohara, K., Kikuchi, T., Shibata, K., et al. (2018). Liquid-like

thermal conduction in intercalated layered crystalline solids. Nat. Mater *17*, 226–230.

17. Zhang, J., Song, L., Pedersen, S.H., Yin, H., Hung, L.T., and Iversen, B.B. (2017). Discovery of high-performance low-cost n-type Mg_3Sb_2-based thermoelectric materials with multi-valley conduction bands. Nat. Commun *8*, 13901.

18. Zhao, L.D., Lo, S.H., Zhang, Y., Sun, H., Tan, G., Uher, C., Wolverton, C., Dravid, V.P., and Kanatzidis, M.G. (2014). Ultralow thermal conductivity and high thermoelectric figure of merit in SnSe crystals. Nature *508*, 373–377.

19. Lee, Y.K., Luo, Z., Cho, S.P., Kanatzidis, M.G., and Chung, I. (2019). Surface oxide removal for polycrystalline SnSe reveals near-single-crystal thermoelectric performance. Joule *3*, 719–731.

20. Chang, C., Wu, M., He, D., Pei, Y., Wu, C.F., Wu, X., Yu, H., Zhu, F., Wang, K., Chen, Y., et al. (2018). 3D charge and 2D phonon transports leading to high out-of-plane ZT in n-type SnSe crystals. Science *360*, 778–783.

21. Zhang, Q., Liao, J., Tang, Y., Gu, M., Ming, C., Qiu, P., Bai, S., Shi, X., Uher, C., and Chen, L. (2017). Realizing a thermoelectric conversion efficiency of 12% in bismuth telluride/skutterudite segmented modules through full-parameter optimization and energy-loss minimized integration. Energy Environ. Sci. *10*, 956–963.

22. Qiu, P., Mao, T., Huang, Z., Xia, X., Liao, J., Agne, M.T., Gu, M., Zhang, Q., Ren, D., Bai, S., et al. (2019). High-efficiency and stable thermoelectric module based on liquid-like materials. Joule *3*, 1538–1548.

23. Burton, M.R., Mehraban, S., Beynon, D., McGettrick, J., Watson, T., Lavery, N.P., and Carnie, M.J. (2019). 3D printed SnSe thermoelectric generators with high figure of merit. Adv. Energy Mater *9*, 1900201.

24. Jood, P., Ohta, M., Yamamoto, A., and Kanatzidis, M.G. (2018). Excessively doped PbTe with Ge-induced nanostructures enables high-efficiency thermoelectric modules. Joule *2*, 1339–1355.

25. Perumal, S., Roychowdhury, S., and Biswas, K. (2016). High performance thermoelectric materials and devices based on GeTe. J. Mater. Chem. C *4*, 7520–7536.

26. Fu, C., Bai, S., Liu, Y., Tang, Y., Chen, L., Zhao, X., and Zhu, T. (2015). Realizing high figure of merit in heavy-band p-type half-Heusler thermoelectric materials. Nat. Commun *6*, 8144.

27. Arabbagheri, S. (2015). Präparative Untersuchung an Thermoelektrischen Materialien, PhD Dissertation (Universität Regensburg).

28. Nakajima, S. (1963). The crystal structure of $Bi_2Te_{3-x}Se_x$. J. Phys. Chem. Solids *24*, 479–485.

29. Batsanov, S.S. (2001). Van der Waals radii of elements. Inorg. Mater *37*, 871–885.

30. Setyawan, W., and Curtarolo, S. (2010). High-throughput electronic band structure calculations: challenges and tools. Comp. Mater. Sci. *49*, 299–312.

31. Zhao, L.D., He, J., Hao, S., Wu, C.I., Hogan, T.P., Wolverton, C., Dravid, V.P., and Kanatzidis, M.G. (2012). Raising the thermoelectric performance of p-type PbS with endotaxial nanostructuring and valence-band offset engineering using CdS and ZnS. J. Am. Chem. Soc. *134*, 16327–16336.

32. Wang, H., Pei, Y., LaLonde, A.D., and Snyder, G.J. (2011). Heavily doped p-type PbSe with high thermoelectric performance: an alternative for PbTe. Adv. Mater. Weinheim *23*, 1366–1370.

33. Roisnel, T., and Rodríquez-Carvajal, J.R. (2001). WinPLOTR: a windows tool for powder diffraction pattern analysis. Mater. Sci. Forum *378–381*, 118–123.

34. Ma, Y., Hao, Q., Poudel, B., Lan, Y., Yu, B., Wang, D., Chen, G., and Ren, Z. (2008). Enhanced thermoelectric figure-of-merit in p-type nanostructured bismuth antimony tellurium alloys made from elemental chunks. Nano Lett. *8*, 2580–2584.

35. Santos, R., Yamini, S.A., and Dou, S.X. (2018). Recent progress in magnesium-based thermoelectric materials. J. Mate Chem. A *6*, 3328–3341.

36. Xie, H., Wang, H., Pei, Y., Fu, C., Liu, X., Snyder, G.J., Zhao, X., and Zhu, T. (2013). Beneficial contribution of alloy disorder to electron and phonon transport in half-heusler thermoelectric materials. Adv. Funct. Mater *23*, 5123–5130.

37. Caillat, T., Borshchevsky, A., and Fleurial, J.-P. (1996). Properties of single crystalline semiconducting $CoSb_3$. J. Appl. Phys. *80*, 4442–4449.

38. Al Rahal Al Orabi, R., Mecholsky, N.A., Hwang, J., Kim, W., Rhyee, J.S., Wee, D., and Fornari, M. (2016). Band degeneracy, low thermal conductivity, and high thermoelectric figure of merit in SnTe–CaTe alloys. Chem. Mater *28*, 376–384.

39. Zheng, G., Su, X., Xie, H., Shu, Y., Liang, T., She, X., Liu, W., Yan, Y., Zhang, Q., Uher, C., et al. (2017). High thermoelectric performance of p-BiSbTe compounds prepared by ultra-fast thermally induced reaction. Energy Environ. Sci. *10*, 2638–2652.

40. Zhao, L.D., Wu, H.J., Hao, S.Q., Wu, C.I., Zhou, X.Y., Biswas, K., He, J.Q., Hogan, T.P., Uher, C., Wolverton, C., et al. (2013). All-scale hierarchical thermoelectrics: MgTe in PbTe facilitates valence band convergence and suppresses bipolar thermal transport for high performance. Energy Environ. Sci. *6*, 3346–3355.

41. Yang, D., Yao, W., Chen, Q., Peng, K., Jiang, P., Lu, X., Uher, C., Yang, T., Wang, G., and Zhou, X. (2016). $Cr_2Ge_2Te_6$: high thermoelectric performance from layered structure with high symmetry. Chem. Mater *28*, 1611–1615.

42. Lefèvre, R., Berthebaud, D., Lebedev, O., Pérez, O., Castro, C., Gascoin, S., Chateigner, D., and Gascoin, F. (2017). Layered tellurides: stacking faults induce low thermal conductivity in the new $In_2Ge_2Te_6$ and thermoelectric properties of related compounds. J. Mater. Chem. A *5*, 19406–19415.

43. Van de Walle, C.G., and Neugebauer, J. (2004). First-principles calculations for defects and impurities: applications to III-nitrides. J. Appl. Phys. *95*, 3851–3879.

44. Huang, L.F., and Zeng, Z. (2015). Roles of mass, structure, and bond strength in the phonon properties and lattice anharmonicity of single-layer Mo and W dichalcogenides. J. Phys. Chem. C *119*, 18779–18789.

45. Mounet, N., and Marzari, N. (2005). First-principles determination of the structural, vibrational and thermodynamic properties of diamond, graphite, and derivatives. Phys. Rev. B *71*, 205214.

46. Cao, G., Liu, H., Liang, J., Cheng, L., Fan, D., and Zhang, Z. (2018). Rhombohedral Sb_2Se_3 as an intrinsic topological insulator due to strong van der Waals interlayer coupling. Phys. Rev. B *97*, 075147.

47. Toberer, E.S., Zevalkink, A., and Snyder, G.J. (2011). Phonon engineering through crystal chemistry. J. Mater. Chem. *21*, 15843–15852.

48. Li, W., Lin, S., Ge, B., Yang, J., Zhang, W., and Pei, Y. (2016). Low sound velocity contributing to the high thermoelectric performance of Ag_8SnSe_6. Adv. Sci. *3*, 1600196.

49. Yang, R., Chen, G., and Dresselhaus, M.S. (2005). Thermal conductivity modeling of core−shell and tubular nanowires. Nano Lett. *5*, 1111–1115.

50. Hu, M., Giapis, K.P., Goicochea, J.V., Zhang, X., and Poulikakos, D. (2011). Significant reduction of thermal conductivity in Si/Ge core− shell nanowires. Nano Lett. *11*, 618–623.

51. Zhang, G., Wang, W., and Li, X. (2008). Enhanced thermoelectric properties of core/shell heterostructure nanowire composites. Adv. Mater *20*, 3654–3656.

52. Ibáñez, M., Zamani, R., Gorsse, S., Fan, J., Ortega, S., Cadavid, D., Morante, J.R., Arbiol, J., and Cabot, A. (2013). Core–shell nanoparticles as building blocks for the bottom-up production of functional nanocomposites: PbTe–PbS thermoelectric properties. ACS Nano *7*, 2573–2586.

53. Ibáñez, M., Korkosz, R.J., Luo, Z., Riba, P., Cadavid, D., Ortega, S., Cabot, A., and Kanatzidis, M.G. (2015). Electron doping in bottom-up engineered thermoelectric nanomaterials through HCl-mediated ligand displacement. J. Am. Chem. Soc. *137*, 4046–4049.

54. Zhu, Y., Ophus, C., Toloczko, M.B., and Edwards, D.J. (2018). Towards bend-contour-free dislocation imaging via diffraction contrast STEM. Ultramicroscopy *193*, 12–23.

55. Kim, S.I., Lee, K.H., Mun, H.A., Kim, H.S., Hwang, S.W., Roh, J.W., Yang, D.J., Shin, W.H., Li, X.S., Lee, Y.H., et al. (2015). Thermoelectrics. Dense dislocation arrays embedded in grain boundaries for high-performance bulk thermoelectrics. Science *348*, 109–114.

56. Ploog, K., Stetter, W., Nowitzki, A., and Schönherr, E. (1976). Crystal growth and structure determination of silicon telluride Si_2Te_3. Mater. Res. Bull. *11*, 1147–1153.

57. Bailey, L.G. (1966). Preparation and properties of silicon telluride. J. Phys. Chem. Solids *27*, 1593–1598.

58. Harwell, J.R., Baikie, T.K., Baikie, I.D., Payne, J.L., Ni, C., Irvine, J.T.S., Turnbull, G.A., and Samuel, I.D.W. (2016). Probing the energy levels of perovskite solar cells via Kelvin probe and UV ambient pressure photoemission spectroscopy. Phys. Chem. Chem. Phys. *18*, 19738–19745.

59. Faleev, S.V., and Léonard, F. (2008). Theory of enhancement of thermoelectric properties of materials with nanoinclusions. Phys. Rev. B *77*, 214304.

60. Nishio, Y., and Hirano, T. (1997). Improvement of the efficiency of thermoelectric energy conversion by utilizing potential barriers. Jpn. J. Appl. Phys. *36*, 170–174.

61. Yang, H., Bahk, J.H., Day, T., Mohammed, A.M., Snyder, G.J., Shakouri, A., and Wu, Y. (2015). Enhanced thermoelectric properties in bulk nanowire heterostructure-based nanocomposites through minority carrier blocking. Nano Lett. *15*, 1349–1355.

62. Burke, P.G., Curtin, B.M., Bowers, J.E., and Gossard, A.C. (2015). Minority carrier barrier heterojunctions for improved thermoelectric efficiency. Nano Energy *12*, 735–741.

63. Chen, Z.G., Shi, X., Zhao, L.D., and Zou, J. (2018). High-performance SnSe thermoelectric materials: progress and future challenge. Prog. Mater. Sci. *97*, 283–346.

64. Lan, J.L., Liu, Y.C., Zhan, B., Lin, Y.H., Zhang, B., Yuan, X., Zhang, W., Xu, W., and Nan, C.W. (2013). Enhanced thermoelectric properties of Pb-doped BiCuSeO ceramics. Adv. Mater. Weinheim *25*, 5086–5090.

65. Deng, R., Su, X., Zheng, Z., Liu, W., Yan, Y., Zhang, Q., Dravid, V.P., Uher, C., Kanatzidis, M.G., and Tang, X. (2018). Thermal conductivity in $Bi_{0.5}Sb_{1.5}Te_{3+x}$ and the role of dense dislocation arrays at grain boundaries. Sci. Adv. *4*, eaar5606.